Review

Nanoplasmon–Semiconductor Hybrid for Interface Catalysis

Jingang Wang [1],[†] ![ORCID]**, Naixing Feng [2],[†]** ![ORCID]**, Ying Sun [3] and Xijiao Mu [4],***

1   College of Sciences, Liaoning Shihua University, Fushun 113001, China; Jingang_wang@lnpu.edu.cn
2   College of Electronic Science and Technology, Shenzhen University, Shenzhen 518060, China; fengnaixing@gmail.com
3   College of Chemistry, Liaoning University, Shenyang 110036, China; sunying024chem@163.com
4   School of Mathematics and Physics, Beijing Key Laboratory for Magneto-Photoelectrical Composite and Interface Science, University of Science and Technology Beijing, Beijing 100083, China
*   Correspondence: shumuxijiao@163.com; Tel.: +86-180-4003-6755
†   Contributed Equally.

![check for updates]

Abstract: We firstly, in this review, introduce the optical properties of plasmonic metals, and then focus on introducing the unique optical properties of the noble metal–metal-oxide hybrid system by revealing the physical mechanism of plasmon–exciton interaction, which was confirmed by theoretical calculations and experimental investigations. With this noble metal–metal-oxide hybrid system, plasmonic nanostructure–semiconductor exciton coupling interactions for interface catalysis has been analyzed in detail. This review can provide a deeper understanding of the physical mechanism of exciton–plasmon interactions in surface catalysis reactions.

Keywords: surface plasmon; local surface plasmon; SERS; TERS; PSPP

---

1. Introduction

Surface plasmons (SPs) are coherent collective electrons oscillating along the interface where the signs of the real part of the dielectric function are different in the two sides [1]. Specifically, localized surface plasmons (LSPs) have been broadly applied in the fields of surface plasmon resonance sensors [2], surface-enhanced Raman scattering (SERS) [3], tip-enhanced Raman scattering (TERS) [4], and plasmonic photodetector [5].

Nowadays, the novel applications of SPs in surface catalysis, such as photocatalysis, have been extensively investigated [6–18]. To use solar energy in photocatalytic applications more efficiently, understanding the internal mechanism of SPs is of paramount importance. In most cases, with a properly designed nanostructure that is usually efficient in light-trapping [19,20], localized surface plasmon resonance (LSPR) can occur where the confined free electrons oscillate with the same frequency as the incident radiation and lead to a highly and intense localized electromagnetic field. Based on this phenomenon, SERS has been broadly studied, where the Raman signals can be enhanced over a large frequency range. After light absorption and LSPR excitation, the accumulated energy is transferred to electrons in the conduction band. Highly energetic electrons generated from plasmon decay are named as "hot electrons", and these are a critical part in driving the surface catalysis; thus, not only is the energy to overcome the reaction barrier produced but also electrons for reduction catalysis are obtained. Further, by using propagating surface plasmon polaritons (PSPPs), the damages caused by direct incident lasers can also be avoided. Hence, plasmon-driven surface catalysis has several outstanding merits, e.g., the extremely high surface sensitivity and improved catalytic efficiency [21]. However, according to the catalysis dynamics investigated by ultrafast transient absorption spectroscopy,

the lifetime of the hot electrons is relatively short and this is the major challenge for plasmon-induced hot-electron-transfer catalysis. Thermo-plasmonics has important implications for surface catalysis and chemical processes [22].

Metal oxides have emerged as potential candidates for solving these problems. For example, monolayer MoS_2, a two-dimensional material with a direct band gap of 1.8 eV [23,24], has a wide range of electronic, mechanical, thermal, optical, and chemical properties that have attracted a significant amount of attention [25]. Monolayer MoS_2 has a high transparency (>92%) in the visible light region, large surface-to-bulk ratio, quantum confinement effects, and high potential for promoting surface catalysis [23]. Furthermore, an MoS_2 monolayer can efficiently protect plasmonic metals (usually Ag) from rapid oxidation.

However, low yield of hot electrons and the large band gaps limit the applications of metal-oxides in catalysis. However, TiO_2 in particular has been attracting much interest in the photocatalytic field as an outstanding electron-accepting metal-oxide. The conduction band of TiO_2 has a high density of states. Because of its merits, TiO_2 has the ability to permit fast electron injection. Extensive studies have investigated the hybrid systems consisting of Au or Ag NPs with TiO_2 [26–32]. According to transient absorption spectroscopy [33–35], TiO_2 has many outstanding optical properties that make it superior to dye-sensitized semiconductors, such as SnO_2, ZnO [36,37], and In_2O_3. Many studies attempted to improve its photocatalytic efficiency [38–40], and the catalysis dynamics of TiO_2 photocatalytic reactivity have been investigated extensively [41–45].

Moreover, its thermal stability, photostability, low cost, and harmlessness make TiO_2 a highly robust competitor. However, TiO_2 has some drawbacks, including the large band gap of 3.3 eV, which limits the photo-absorption in the UV region of the solar spectroscopy [46–49]. Another crucial obstacle is the charge-charge recombination in metal-oxides, whose rate should be reduced to improve the catalysis efficiency [47,50]. The recombination results in an overall loss of the charge carriers before they reach the surface, and can be addressed by maximizing photon absorption with the help of plasmonic nanostructures [51].

The results of experiments in recent years can be seen from the Table 1.

Table 1. The table demonstrates results of plasmon–exciton coupling for catalysis.

The Coupling of Plasmon-Exciton for Surface Catalysiss			
Date \ Materials	Graphene + Metal	TiO_2 + Metal	MoS_2 + Metal
2015	Plasmon + graphene for catalysis	Plasmon + TiO_2	
2016	Ultrafast Plasmon-Exciton Interaction of Ag Nanowire-Graphene	Ultrafast Plasmon on Ag/TiO_2	
2017	Plasmon–Exciton-Co-driven catalysis Reactions	Ag nanoparticles-TiO_2 film hybrid for catalysis	MoS_2-Ag nanoparticles hybrids for catalysis
2018	Electrically enhanced hot hole driven oxidation catalysis		Femtosecond dynamics of MoS_2-Ag nanoparticles hybrid

2. Mechanisms

Cavity quantum electrodynamics (QED) is the proper mechanical description to study the quantum interactions between light and matter inside a microcavity. Taking an excited isolated atom for example, there is no effective mechanism, which leads to electron decay due to the two orthogonal eigenstates (ground and excited levels). However, Purcell discovered that the spontaneous emission is not only related to the emitter but also depends on environments, which can be confirmed by the case in which an atom is inside the cavity with perfectly reflecting walls. Based on this theory, we can consider the emitter and its environment as a whole system.

Although the connection between plasmonic nanostructures and a semiconductor forms a metal–semiconductor Schottky junction [20], combining the merits of noble metals and metal-oxides is a promising way to optimize photocatalytic devices by addressing several limitations, and to further improve the surface catalytic efficiency. The lifetime of hot electrons is obviously prolonged from the femtosecond scale to the picosecond scale, which is vital in driving the surface catalysis confirmed by Ding and coworkers with the fabricated graphene-Ag NPs system [52].

On the other hand, the band gaps of metal oxides are decreased and the density of states (DOS) is adjusted for improving the efficiency of hybrid structures. The localized SPR effect induced by plasmonic nanostructures can increase photon absorption due to the confined field enhancement. Understanding the internal mechanism and tenability of these hybrid systems, still experimentally and theoretically challenging subjects, is important for further investigations of the dynamics and various applications.

When excitons of metal-oxides strongly couple to the localized SPs, the novel hybridized energy states form plexcitons (also exciton-polaritons) as a type of polariton. Several studies have reported the optical advanced properties of plexcitonic nanostructures [53–57]. Importantly, the hybrid systems already have many applications such as in chemical sensors, pH meters [58], light harvesting [59], and optically active devices [60,61].

Hence, the mechanism of plasmon–exciton coupling interactions with the semi-classical theory and quantum theory will be introduced for deeper understanding of the unique properties of noble metal–metal-oxide hybrid systems. Further, the merits of the hybrid system will be confirmed experimentally and theoretically, by analyzing the ultrafast transient absorption and plasmon–exciton co-driven catalysis.

2.1. Free-Space Spontaneous Emission

To illustrate the basic physical mechanism underlying spontaneous emission, we first consider the electric dipole interaction between the single two-level system and the single mode of the electromagnetic field. The two-level system, which is formally analogous to a spin-1/2 system with two possible states, can be conveniently described by the Hamiltonian:

$$H_a = \hbar\omega_e |e\rangle\langle e| + \hbar\omega_g |g\rangle\langle g| \tag{1}$$

where $\hbar\omega_e$ and $\hbar\omega_g$ are the energies of the excited and the ground levels, respectively. The wave function of the two-level atom can be described as $|\psi(t)\rangle = C_e(t)|e\rangle + C_g(t)|g\rangle$, where C_e and C_g are the probability amplitudes of finding the atom in states $|e\rangle$ and $|g\rangle$ which represent the upper and lower level states of the atom, respectively.

In the absence of any interaction, an atom initially in its excited state $|e\rangle$ will remain there at all times. Transitions between the eigenstates of the atom result from the coupling of the atom to some other system. In the case of dipole coupling to a single electromagnetic field mode of frequency ω_c, the total atom-field system can be described by the Jaynes–Cummings Hamiltonian:

$$H_s = H_a + H_f + H_{a-f} \tag{2}$$

where $H_f = \hbar\omega_c a^\dagger a$ and the annihilation and creation operators a and $a^\dagger$ obey the boson commutation relation $[a, a^\dagger] = 1$. In the dipole and rotating wave approximation, the interaction Hamiltonian (H_{a-f}) between this field mode and the two-level atom can be described as follows:

$$H_{a-f} = -\hat{d} \cdot \hat{E} \tag{3}$$

where $\hat{d}$ is the dipole moment operator of the transition, and $\hat{E}$ is the electric field operator related to the polarization of the field mode. Hence, the total atom-field system in Equation (2) can be re-expressed as follows:

$$H = E_0 + \hbar\omega_0\sigma_z + \hbar\omega_c a^\dagger a + \hbar g(R)a^\dagger\sigma_- + h.c \qquad (4)$$

where $\omega_0 \equiv \omega_e - \omega_g$ is the atomic transition frequency, and g is half the so-called vacuum Rabi frequency. The vacuum Rabi frequency $2g(\hat{R})$ normally depends on the location $\hat{R}$ of the atom. The interaction is physically transparent: the atom can either absorb a photon and undergo a transition towards the excited state, or it can emit a photon when undergoing a transition from the excited to the ground state. Within the framework based on the Jaynes–Cummings model, the excitation number in the atom-field system is conserved. On the resonance ($\omega_c = \omega_0$), when the frequency of single electromagnetic field mode equals the frequency of atom transition, the time-dependent states of atom-field system are as follows:

$$|\psi(0)\rangle = \cos(gt)|e,0\rangle - i\sin(gt)|g,1\rangle \qquad (5)$$

Therefore, the probability $P_g(t)$ for the atom to be in its ground electronic state $|g\rangle$ is as follows:

$$P_g(t) = |\langle g, 1|\psi(t)\rangle|^2 = \sin^2(gt) \qquad (6)$$

The equation can simply demonstrate the form of spontaneous emission: the quantized field (fluctuation) in the vacuum induces transitions between the two states. Further, the puzzling oscillatory behavior of $P_g(t)$ at the "vacuum Rabi frequency" $2g$ can also be presented by the simple model, which results from the periodic exchange between the atom and cavity.

Based on Fermi's golden rule, the transition rate of corresponding radiation from an excited state towards the lower energy level can be calculated as follows:

$$\gamma = \frac{2\pi}{\hbar^2}\left|\left\langle f\left|\hat{\mu} \cdot \hat{E}\right|i\right\rangle\right|^2 \rho(\omega) \qquad (7)$$

In the equation, γ represents the transition decay rate from the initial (excited) state $|i\rangle$ to the final state $|f\rangle$. $\hat{\mu}$ and $\hat{E}$ are the electric dipole and vacuum-field operators, respectively. $\rho(\omega)$ represents the final photonic density of states, and the decay rate of the excited atomic state population in the free space can be represented as follows:

$$\gamma_{free} = \frac{1}{\tau_{free}} = \frac{\mu_{if}^2\omega^3}{3\pi\varepsilon_0\hbar c^3} \qquad (8)$$

based on $\left|\langle f|\hat{\mu}\cdot\hat{E}|i\rangle\right|^2 = \frac{1}{3}\mu_{if}^2 E_{vac}^2$, where τ_{free} is the radiative lifetime and $E_{vac} = \sqrt{(\hbar\omega)/2\varepsilon_0 V}$ [62–66].

2.2. Spontaneous Emission in Cavities

The Hamiltonian of a system that consists of an atom coupling to a single mode field can be described as $H_s = H_a + H_f + H_{a-f}$. The atom-cavity mode system has two dissipative processes: to the free space electromagnetic field background or to the outside world due to the mirror losses and diffraction. Further, the master equation of the atom-cavity mode can be described as follows:

$$\dot{\rho}_s = -\frac{i}{\hbar}\left[H_{eff}\rho - \rho H_{eff}^\dagger\right] + \kappa a\rho_s a^\dagger + \gamma'\sigma_-\rho_s\sigma_+ \qquad (9)$$

where $H_{eff} = H_s + H_{loss}$ and $H_{loss} = -i\hbar\frac{\gamma'}{2}\sigma_+\sigma_- - i\hbar\frac{\kappa}{2}a^\dagger a$. According to the master Equation (8), the evolution of the state can be presented as follows:

$$i\hbar\frac{d|\psi(t)\rangle}{dt} = H_{eff}|\psi(t)\rangle \qquad (10)$$

where the state can be introduced as $|\psi(t)\rangle = C_e(t)e^{\frac{1}{2}\delta t}|e,0\rangle + C_g(t)e^{\frac{1}{2}\delta t}|g,1\rangle$.

The coupling between LSPs and excitons results from the coherent dipole-dipole interaction [67]. Based on the brief introduction of basic concepts, we move forward to distinguishing the different regimes. The interactions could be divided into two different kinds (in the weak or strong coupling regime) by the lifetime of the LSPs and excitons. When the system is in the weak coupling regime, the lifetime of plasmonic resonance is relatively short compared with the spontaneous decay rate of the isolated emitter. In contrast, when the lifetime of LSPR is much longer, then it is in the limit of strong coupling.

In other ways, regimes can also be determined by comparing the three typical constants.

1. The dipole coupling constant between the atom and the cavity mode g;
2. The decay rate of the mode κ;
3. The rate of spontaneous emission into electromagnetic field modes γ'.

When κ and γ' overwhelm the Hamiltonian dipole interaction represented by $g(g \ll \kappa, \gamma')$, the system is in the weak coupling regime. In the limit regime, the role of the vacuum field is considered as a perturbation to the emitter, where the cavity and emitter can be separately treated. In contrast, the system is in the strong coupling regime if $g \gg \kappa, \gamma'$. In this limit regime, the emitter and cavity can only be treated as a system, and can only be described with quantum electrodynamics treatment.

2.2.1. Weak Coupling

The interaction between matter and light in the weak coupling regime, is not stronger than that outside the system, for example, the fast relaxation of LSPs [67,68]. LSPs can modify the absorption cross-section due to plasmonic nanostructures. The final density of states, for instance, is maximum at the plasmon resonance wavelength when the emitter is near metal NPs. When the cavity has only one mode of frequency ω_c, $\rho(\omega)$ can be described as follows:

$$\rho(\omega) = \frac{2}{\pi} \frac{\Delta\omega}{4(\omega - \omega_c)^2 + \Delta\omega^2} \tag{11}$$

which represents the density of states and can be influenced by the quality factor of cavity $Q = \omega_c/\Delta\omega$. Further, according to Equation (11), it is obvious to find the local density of states (LDOS) maximum at $\omega = \omega_c$ [69]. In addition, the decay rate of an emitter placed within a plasmonic cavity can be calculated as follows:

$$\gamma_{cav} = \beta^2 \frac{2\mu_{if}^2}{\varepsilon_0 \hbar} \frac{Q}{V} \tag{12}$$

Using the Purcell factor F_P [69–71], the effect of cavity on the decay rate of the emitter can be described. The spontaneous decay rate is enhanced If $F_P > 1$, otherwise, the cavity can inhibit the emission:

$$F_P = \frac{\gamma_{cav}}{\gamma_{free}} = \frac{\tau_{free}}{\tau_{cav}} = \frac{3}{4\pi^2} Q(\frac{\lambda^3}{n^3 V}) \tag{13}$$

Moreover, the overall enhancement in the quantum yield ($\eta = \gamma_{rad}/(\gamma_{rad} + \gamma_{nonrad})$) can be further determined by the competition between radiative and nonradiative rates, and the maximum can be achieved by optimizing the radiative rate enhancements and minimizing the nonradioactive losses [67,72].

2.2.2. Strong Coupling

The new quasiparticle (plexciton) in the strong coupling regime is formed with distinct properties possessed by neither original particle. The coherent coupling interaction between the atom and the cavity mode is so strong that when the photon emitted into the cavity is similar to be reabsorbed before escape (the light and matter exchange energy periodically), and results in two new mixed states

separated energetically (named as Rabi splitting) [68,73,74]. Detailed information can be seen from Figure 1.
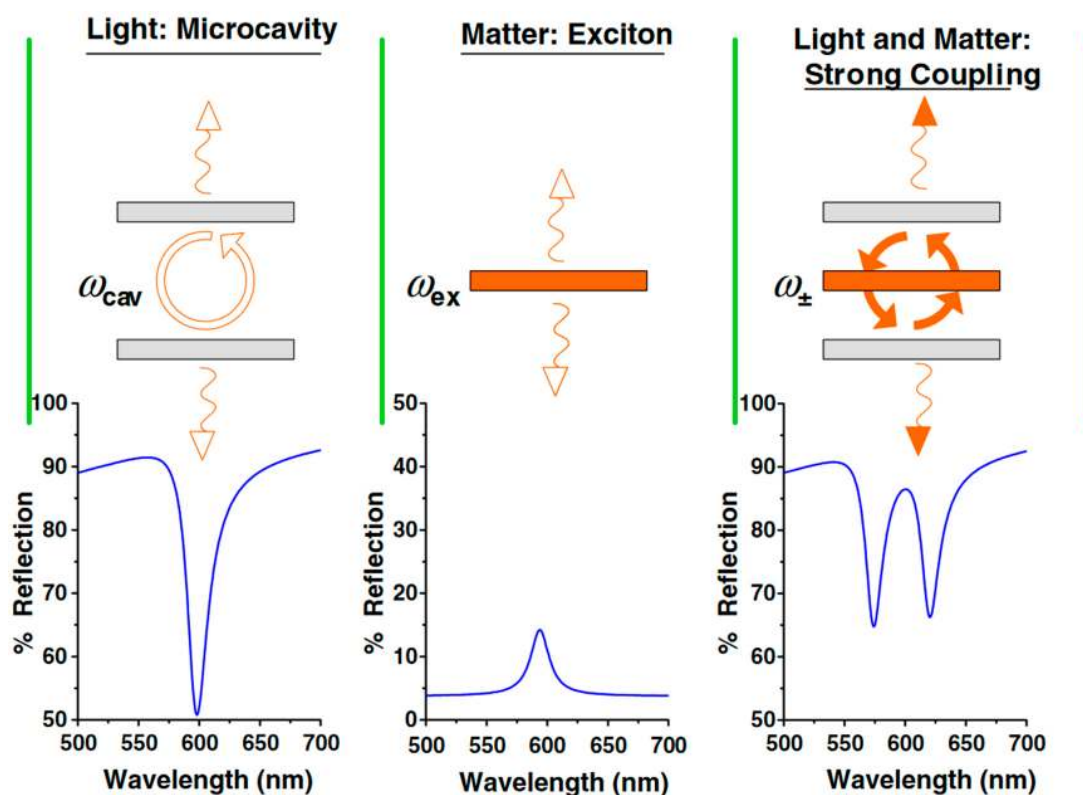

Figure 1. The mechanism of strong coupling between light and matter revealed by reflectance spectra [75].

The perturbative analysis of coupling between the cavity mode and atom ceases to be justified. General solution for arbitrary g, γ', and κ is of the form

$$C_e(t) = C_{e1}e^{\alpha_1 t} + C_{e2}e^{\alpha_2 t} \tag{14}$$

where

$$\alpha_{1,2} = -\frac{1}{2}\left(\frac{\gamma'}{2} + \frac{\kappa}{2} + i\delta\right) \pm \frac{1}{2}\left[\left(\frac{\gamma'}{2} + \frac{\kappa}{2} + i\delta\right)^2 - 4g^2\right]^{1/2} \tag{15}$$

The constants C_{e1} and C_{e2} can be determined from initial conditions $C_e(0) = 1$ and $C_g(0) = 0$, respectively. In the strong coupling regime with $g \gg \kappa, \gamma'$, and δ, it can be adjusted to

$$\alpha_{1,2} = -\frac{1}{2}\left(\frac{\gamma'}{2} + \frac{\kappa}{2} + i\delta\right) \pm ig \tag{16}$$

According to Equation (16), the evolution of the upper state population can be described, as well as the split at the vacuum Rabi frequency.

Based on the Jaynes–Cummings Hamiltonian, the system only has two states: $|e, n\rangle$ and $|g, n+1\rangle$. When the atom-field interaction is considered, the eigenenergies can be described as follows:

$$E_{2n} = \hbar\left(n + \frac{1}{2}\right)\omega_c - \hbar R_n \tag{17}$$

$$E_{1n} = \hbar\left(n + \frac{1}{2}\right)\omega_c + \hbar R_n \tag{18}$$

Here R_n is the n-photon generalized Rabi frequency:

$$R_n = \frac{1}{2}\sqrt{\delta^2 + 4g^2(n+1)} \tag{19}$$

The energies of the state $|e, n\rangle$ and state $|g, n+1\rangle$ cross at $\delta = 0$, but the atom-field interaction removes this degeneracy, causing the dressed states $|1, n\rangle$ and $|2, n\rangle$ to repel each other, or anticross. In other word, the anticrossing corresponds to the resonance condition $\omega_0 = \omega_c$ (a central peak at ω_c and two sidebands at $\omega_c \pm R_n$).

2.3. Femtosecond Absorption

Hot electrons can be generated from plasmon decay in plasmonic nanostructures, which can be treated as efficient light-trapping components and can significantly improve the photocatalytic efficiency of traditional semiconductor devices. The hybrid system of a noble metal and a metal oxide was once considered to have two separate components and electron transfer was considered to be difficult because the individual electrons were not able to get sufficient energy to overcome the Schottky barrier [76]. However, the electron transfer from gold to the TiO_2 electrode had been proved by the generated photocurrent under excitation of the plasmon band [77,78], which is relevant because the wide bandgap of TiO_2 limits the generation of photocurrents. The generated hot electrons will go through three steps: generation, injection, and regeneration. The reverse electron transfer from TiO_2 to gold, as the inverse process, is also proved in core-shell Ag-TiO_2 NPs [79]. Based on the investigations, the energy needed to overcome the reaction barrier in hybrid systems is relatively smaller than the bandgap of TiO_2. Hence, bringing the plasmonic nanostructures in contact with a semiconductor is a promising way to develop photocatalytic devices.

The electromagnetic decay takes places on a femtosecond timescale in plasmonic nanostructures, either radiatively through non-radiatively by transferring the energy to hot electrons or re-emitted photons [80–84].

To further reveal the internal mechanism of the prolonged lifetime of hot electrons in plasmon–exciton coupling interactions, the pump-probe ultrafast transient absorption spectroscopy (UTAS) is usually applied to investigate the timescale of the hot electron transfer process. Among the hot electrons transfer processes, the fast-electron injection into the metal oxide before recombination is crucial for improving the conversion efficiency. Direct evidence of electron transfer from Au NPs to TiO_2 can be obtained. Furube and coworkers revealed the internal mechanism of ultrafast plasmon-induced electron transfer from 10 nm Au NPs to TiO_2 NPs with femtosecond transient absorption spectroscopy [15,85,86], and revealed that the hot electron generation and injection were completed within 50 fs [42,45,87–97]. When the plasmons of gold NPs are excited, the electrons with a non-Fermi distribution undergo relaxation through the re-emission of photons or carrier multiplication within 100 fs due to the electron–electron interaction [52,98,99], electron–phonon interaction at the timescale of 1–10 ps, and phonon–phonon interactions around 100 ps [100,101]. Hence, researchers concluded that the hot electron injection resulted from electron–electron interaction.

The N_3/TiO_2 system, whose carrier injection efficiency is nearly 100%, is used for the comparison of the electron transfer yield [102]. According to the transient absorption intensity ratio between Au/TiO_2 and N_3/TiO_2 (~100% injection efficiency), the electron injection yield in Au/TiO_2 was evaluated to be about 40% under 550 nm excitation.

In addition, the Au/ZrO_2 system is set for monitoring the response of excited Au nanodots as a control group, where no electron is able to transfer from Au nanodots to ZrO_2, since the conduction band edge of ZrO_2 is located 0.9 V above that of TiO_2 [102]. The observed transient absorption of Au/TiO_2 can be attributed to the electron transfer into TiO_2, because there is no transient absorption for Au/ZrO_2 with a probe laser of 3500 nm. Further, the electron transfer was completed within 240 fs, as shown in Figure 2. The timescale of the regeneration process was also investigated by Tian and coworkers [103,104].
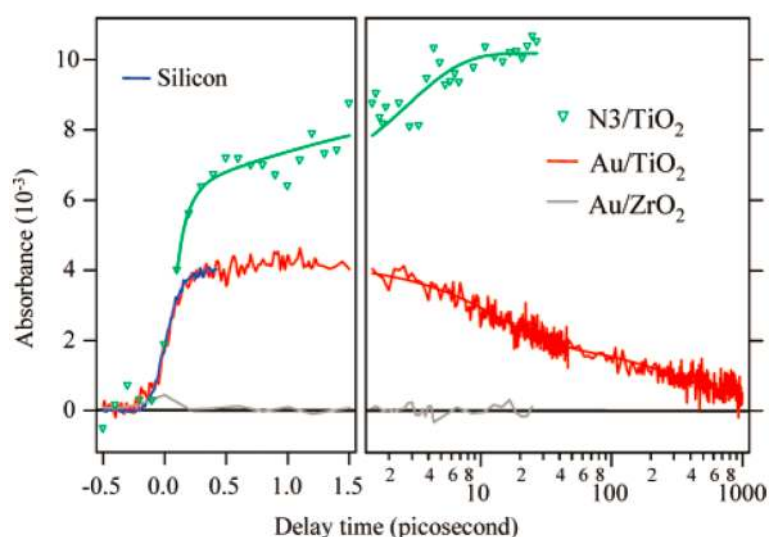
Figure 2. Transient absorption of N_3/TiO_2, Au/TiO_2 and Au/ZrO_2 at 3500 nm [15].

Similarly, an Ag NP–graphene hybrid has also been investigated widely as an appropriate candidate. With the unique properties of graphene, the graphene–Ag nanostructure hybrid systems have been widely applied in investigating plasmon–exciton co-driven surface catalysis, whose mechanism was not clearly elucidated. Ding and coworkers fabricated the graphene-Ag nanowire hybrid system (Figure 3a) to reveal the dynamic process of plasmon–exciton coupling interaction with UTAS, as shown in Figure 3b–e.

The fitted curve in Figure 3c indicates that the lifetime of plasmonic hot electrons is about 3.2 ± 0.8 ps, which is obviously prolonged compared with the situation for isolated Ag NWs (150 fs). Furthermore, graphene cannot only prolong lifetime of the hot electrons dramatically, but also results in the significant accumulations of the hot electrons.

Moreover, the mechanism of exciton–plasmon coupling can also be investigated based on hybrid system of MoS_2-Ag NP, according to the transmission spectra (Figure 4) and ultrafast absorption spectroscopy (Figure 4) results with a pump laser of 400 nm. It is revealed that the enhancement factors of excitonic states of MoS_2 are different; the excitonic state (637 nm) is enhanced significantly with plasmon–exciton coupling interaction, instead of the B excitonic state (595 nm). By comparing the lifetimes of the two excitonic states of MoS_2 (Figure 4), we find that the plasmon–exciton coupling interaction has a strong impact on the lifetime of excitonic states. According to the fitted transient absorption spectra of MoS_2-Ag NP (size of 21 nm) in Figure 4e–h, the lifetime of electron-electron interaction in the hybrid system is enhanced by about 8 times than that of MoS_2 alone. As for the electron–photon interaction, the lifetime is also increased significantly for excitonic states A and B. Hence, it is confirmed that the exciton–plasmon interaction improves the efficiency and probability of catalysis due to the long lifetime of carriers.
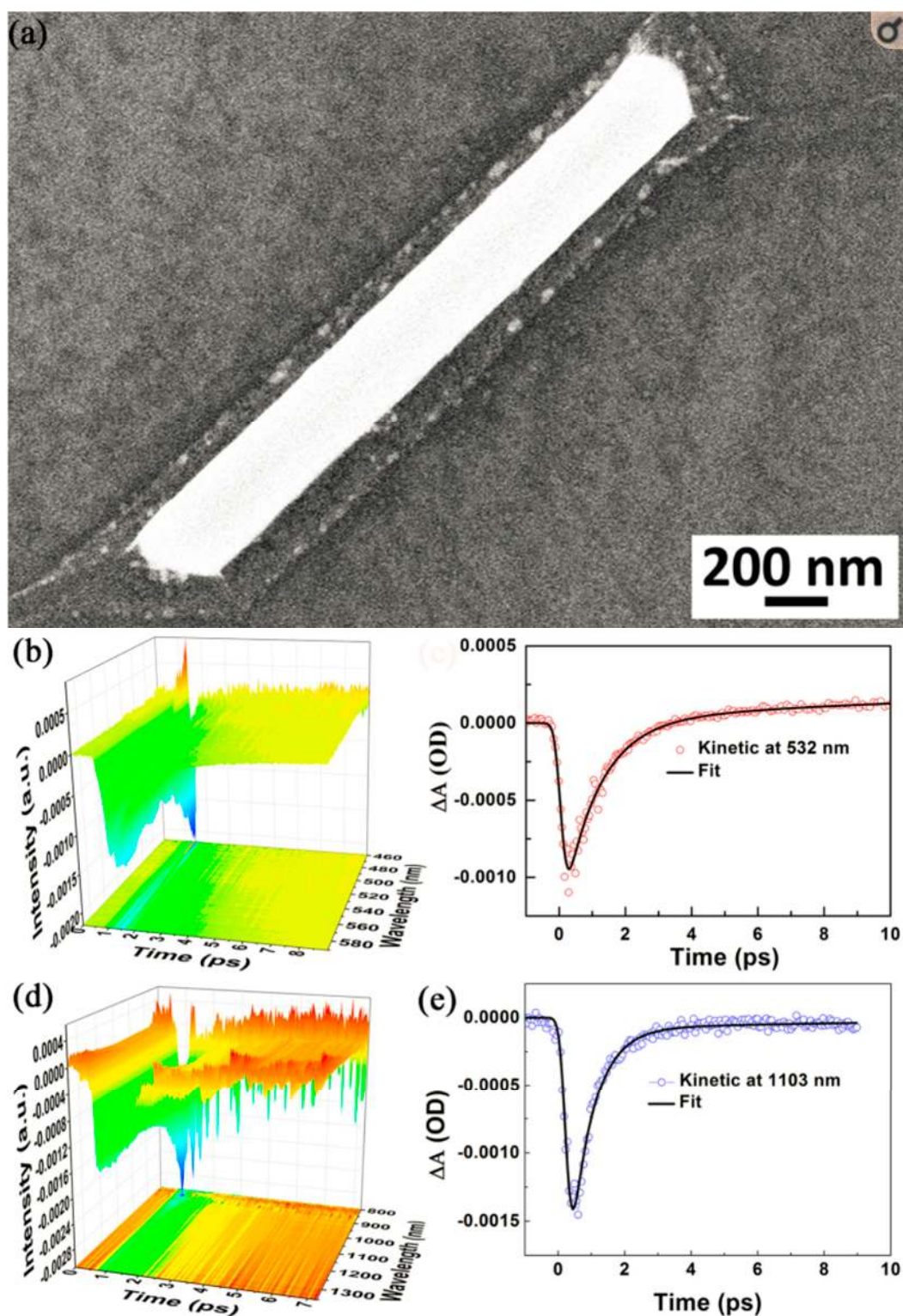
Figure 3. (**a**) The SEM image of Ag NW–graphene hybrid system. (**b**) The corresponding ultrafast pump-probe transient absorption spectroscopy excited by 400 nm, and (**c**) fitted at 532 nm. (**d**) The corresponding ultrafast pump-probe transient absorption spectroscopy excited in NIR region, and (**e**) fitted at 1103 nm [52].
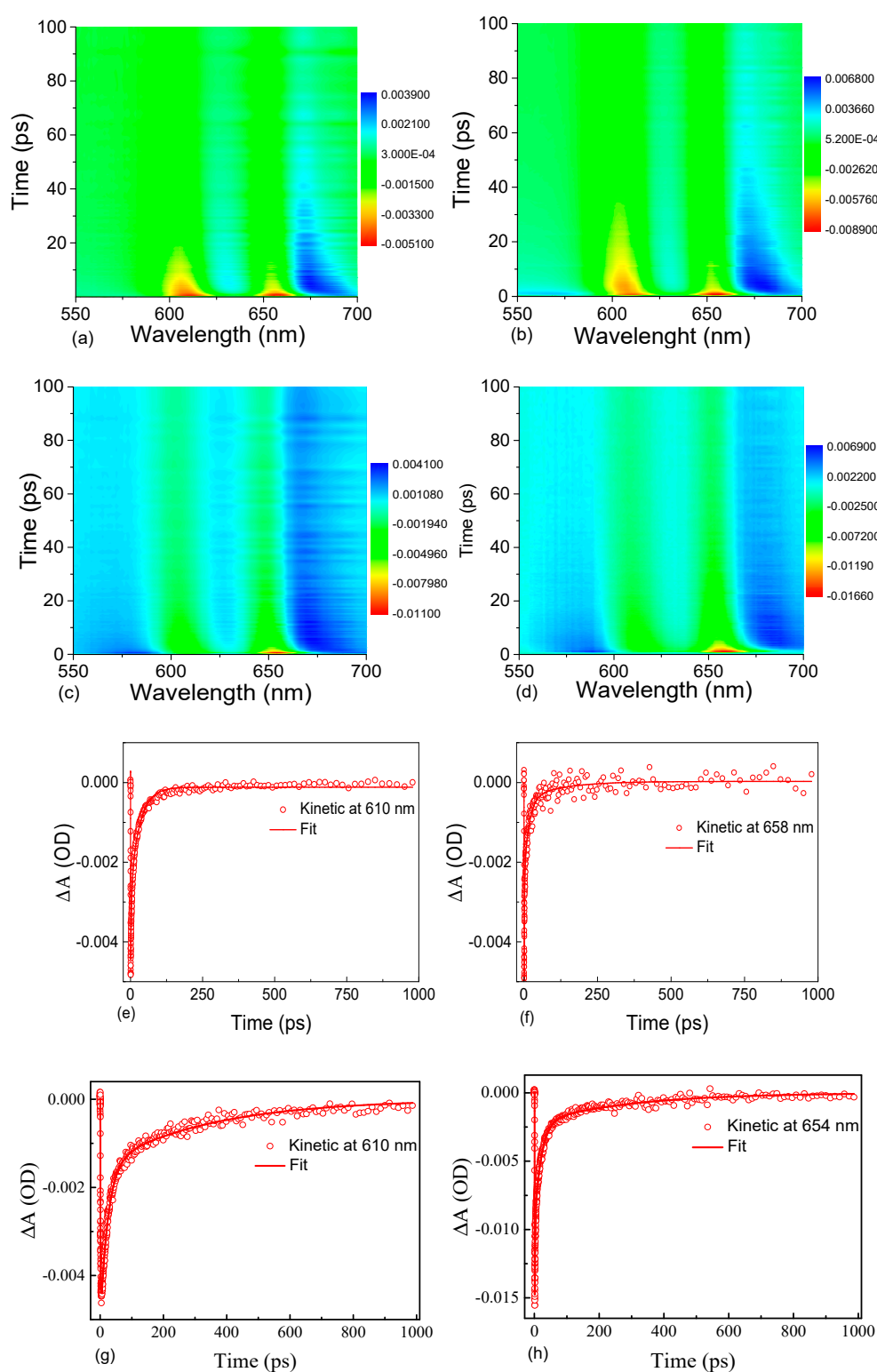
Figure 4. The ultrafast transient absorption spectra of (**a**) monolayer MoS_2, and (**b–d**) monolayer MoS_2-Ag NPs hybrid system where sizes of Ag NPs are 6.1, 14.5 and 21 nm, respectively. The transient absorption spectra of (**e,f**) monolayer MoS_2 fitted at excitonic state A and B respectively, and (**g,h**) monolayer MoS_2-Ag NPs hybrid fitted at excitonic state A and B respectively, where the size of Ag NPs is 21 nm [105].

3. Applications on Photocatalysis

Since 2010, plasmonic hot electrons have been found to be critical in catalysis monitored by the SERS and TERS [12,106,107]. However, based on the investigations, the efficiency of surface plasmon-to-hot electron conversion is considered to be lower than 1% [108]. Hence, several studies attempted to achieve the goal of increasing the efficiency of plasmon-driven surface catalysis.

Before describing the specific application of the hybrid system, we experimentally confirm that the plasmon–exciton coupling degree can be well manipulated, for example, by changing the size of Ag NPs in the Ag NP–TiO_2 film hybrids.

Ding first synthesized a nanosized TiO_2 film on the quartz, with the thickness of ~208 nm and the absorption peak was centered at 524 nm. Above the TiO_2 film, Ag NPs with different sizes were synthesized, as shown in Figure 5. The optimal parameters of components can be studied by UV-Visible absorption spectroscopy, and the ultrafast transfer process of plasmonic hot electron from Ag NPs into TiO_2 film can be investigated by UTAS.
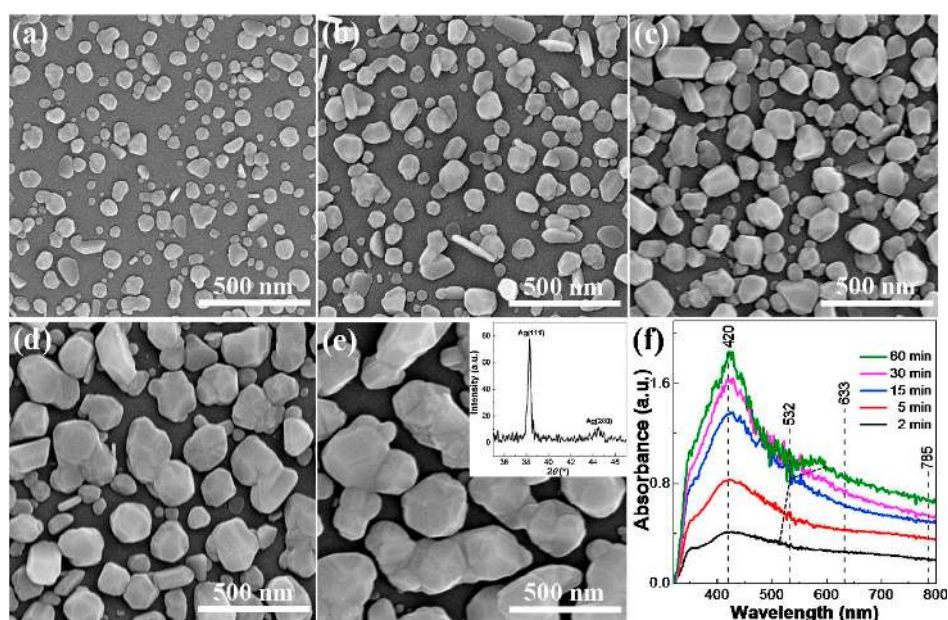

Figure 5. The SEM images of Ag NPs synthesized on TiO_2 film under different UV irradiation for (**a**) 2, (**b**) 5, (**c**) 15, (**d**) 30, and (**e**) 60 min. (**f**) The corresponding in situ real-time UV–vis absorbance spectra of 5(**a**–**e**), respectively [109].

When the Ag NPs are generated under UV irradiation, in addition to the large size, the absorption intensity gradually increases and the strong absorbance peak is red shifted. The strong plasmon–exciton coupling interaction is formed only when the surface plasmon resonance peak of Ag NPs overlaps with the absorption peak of the TiO_2 film (524 nm).

According to the in situ real-time UV-Visible absorbance spectra of hybrid systems (Figure 5), the absorption intensity increases gradually when the UV irradiation time increases from 2 min to 15 min; further, the SPR peak of Ag NPs at 15 min is around 532 nm, while the growth is halted at 30 min and decreases when the time is up to 60 min.

According to the absorption peaks of the Ag NP–TiO_2 film where the Ag NPs were fabricated within 2 min (Figure 6a), there are two ultrafast absorption peaks around 532 nm and 475 nm. Focusing on the case of 532 nm, the electron-electron interaction is about 2 ps while the phonon-electron interaction can approach 71 ps, as shown in Figure 6b. According to the Ag NP size dependent, the ultrafast process of exciton–plasmon interaction of TiO_2 film-Ag NP hybrids in Figure 6c, when the size of Ag NPs increases, the intensity of absorption spectrum become stronger while the lifetime

decreases. The shorter lifetime represents the stronger exciton–plasmon interaction in Ag NP–TiO$_2$ film hybrids. We can conclude that the degree of exciton–plasmon interaction can be well manipulated.
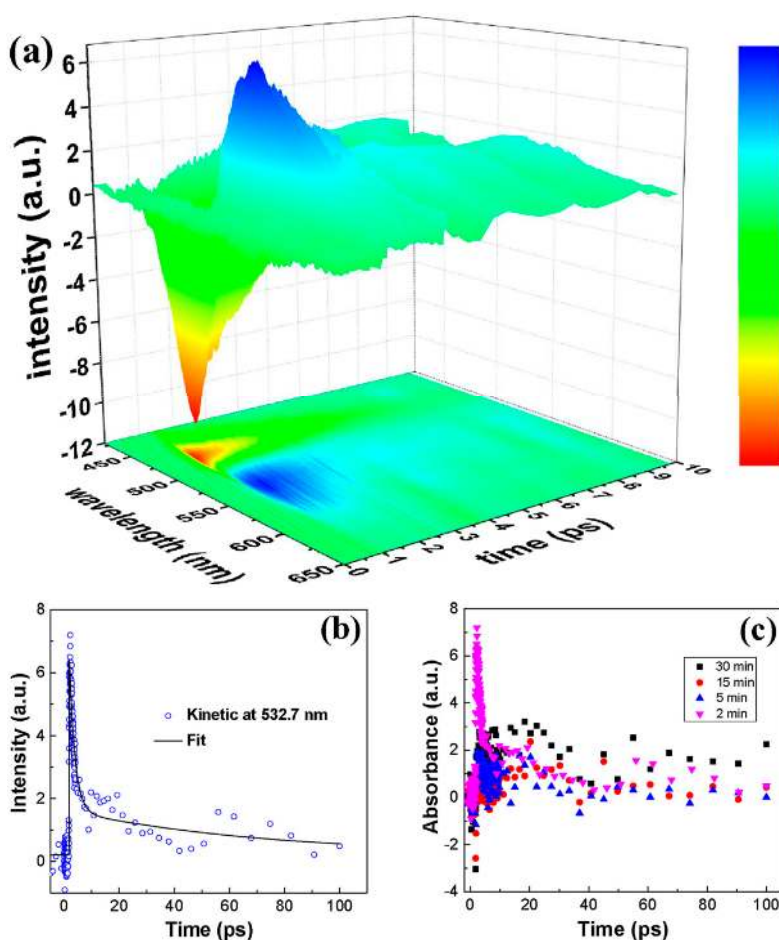

Figure 6. (**a**) The 3D ultrafast transient absorption spectrum of AgNPs-TiO$_2$ film which is synthesized within 2 min, and (**b**) fitted 532.7 nm. (**c**) The ultrafast transient absorption spectra at 532.7 nm for AgNPs-TiO$_2$ film hybrids with different synthesized time [109].

Figure 7a proves again that the superposition between the absorption peak of Ag NPs and TiO$_2$ film can help in monitoring the degree of the coupling interaction, due to the strongest SERS intensity of catalysis of Ag NP–TiO$_2$ film at 15 min.
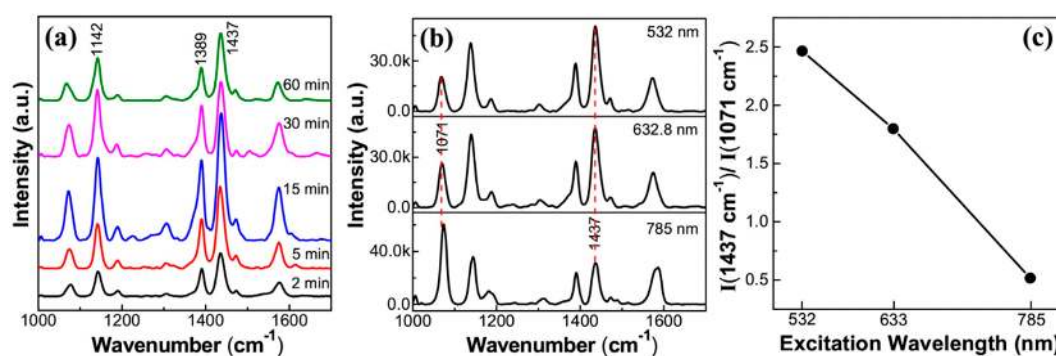

Figure 7. (**a**) The SERS spectra of plasmon-driven oxidation catalysis on AgNPs-TiO$_2$ film with different UV irradiation time. (**b**) Laser wavelength-dependent SERS spectra on 15 min AgNPs-TiO$_2$ film hybrid. (**c**) Relative ratio between intensities at 1437 cm^{-1} and 1071 cm^{-1}, with different excitation wavelengths [109].

The efficiency of the oxidation catalysis can be monitored by the ratio of the intensity at 1437 and 1071 cm^{-1}, where the former is attributed to the Ag mode of DMAB and the latter is attributed to the A1 mode of PATP. The excitation wavelength-dependent oxidation catalysis illustrates that, based on the match between the excitation laser wavelength and SPR peak of Ag NPs, we can obtain the highest yield of the product excited on 532 nm due to the plasmon–exciton coupling interaction. Further, the oxidation catalysis is efficient and stable on the Ag NP–TiO$_2$ film hybrids under different environments, including atmospheric, aqueous, and icy environments [110].

Thus, based on UV–Visible absorption spectroscopy, ultrafast transient absorption spectroscopy, and SERS, the plasmon–exciton coupling interaction in the Ag NP–TiO$_2$ film can be investigated in detail. To obtain the maximum catalytic activity for oxidation catalysis, the degree of coupling interaction can be adjusted by changing the size of Ag NPs and monitoring by the superposition of the SPR peak of Ag NPs and the absorption peak of the TiO$_2$ film.

Yang synthesized monolayer MoS$_2$–Ag NP hybrids where the size of Ag NPs was monitored for shifting LSPR peak to match the exciton energy of monolayer MoS$_2$ and, hence, to further monitor the degree of plasmon–exciton coupling interaction.

As shown in Figure 8, when the size increases, the LSPR peak of Ag NPs is red-shifted, as is the absorption peak of the hybrid system attributed to exciton–plasmon interaction. When they are coupled, LSPR can significantly enhance the excitation rate of the monolayer MoS$_2$ exciton through EM, and the generated collective states result in stronger optical absorption than the individual components.
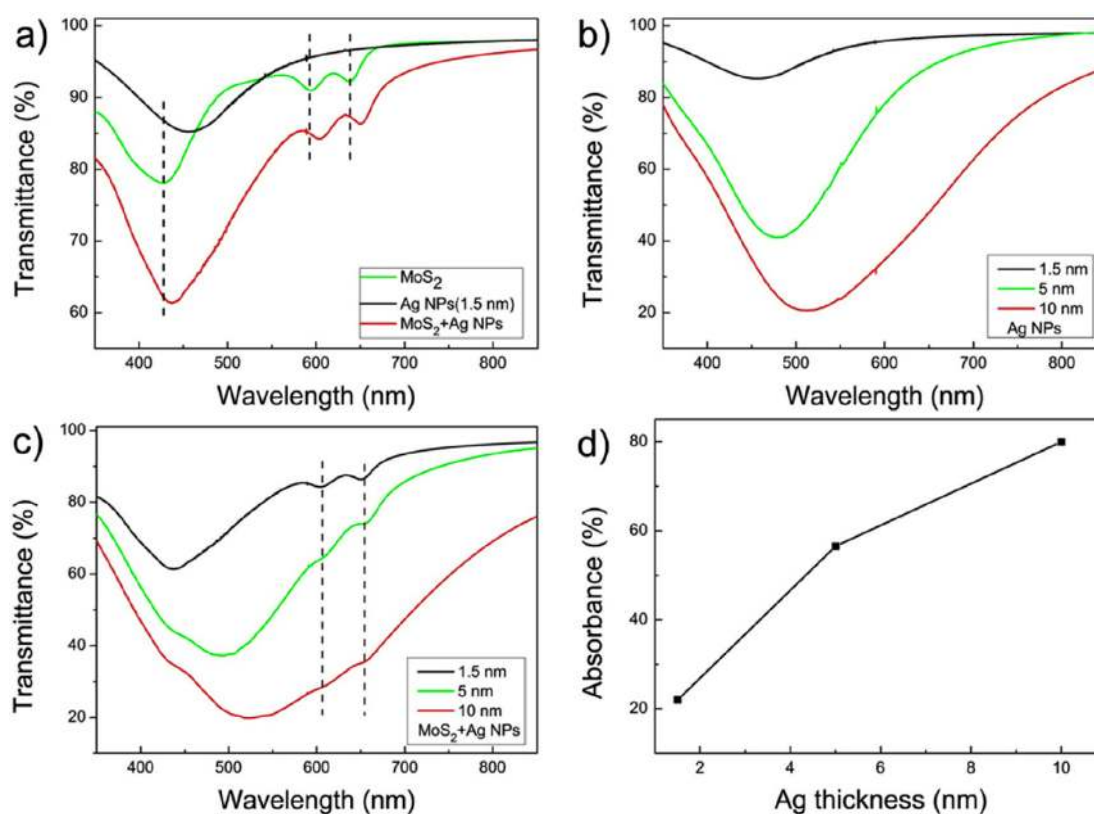

Figure 8. (**a**) The transmission spectra of Ag NPs, monolayer MoS$_2$ and MoS$_2$-Ag NPs hybrids, (**b**) the transmission spectra of Ag NPs with different diameters, (**c**) the transmission spectra of MoS$_2$-Ag NPs hybrids with different sizes of Ag NPs; (**d**) The absorbances for hybrids with different sizes Ag NPs at 532 nm [111].

On the monolayer MoS$_2$ substrate, there is no obvious phenomenon regarding occurring catalysis. With a low-intensity laser, the probability of the reduction catalysis on the Ag NPs substrate is much lower than on the MoS$_2$–Ag NP hybrid system. Further, the advantages of the exciton–plasmon

coupling can be confirmed by investigating the Ag NP size-dependent exciton–plasmon co-driven surface catalysis, as shown in Figure 9. With the help of the strongest exciton–plasmon interaction near 532 nm, and highest probability and efficiency of reduction catalysis can be achieved.

In Figure 10, comparing the ratio between the Raman intensities of reactant (1338 cm^{-1}) and product (1432 cm^{-1}), we can conclude that the probability of the reduction catalysis for 4NBT adsorbed on Ag NPs directly is much lower than that on the MoS$_2$–Ag NP hybrid substrate, which supports the aforementioned conclusion.
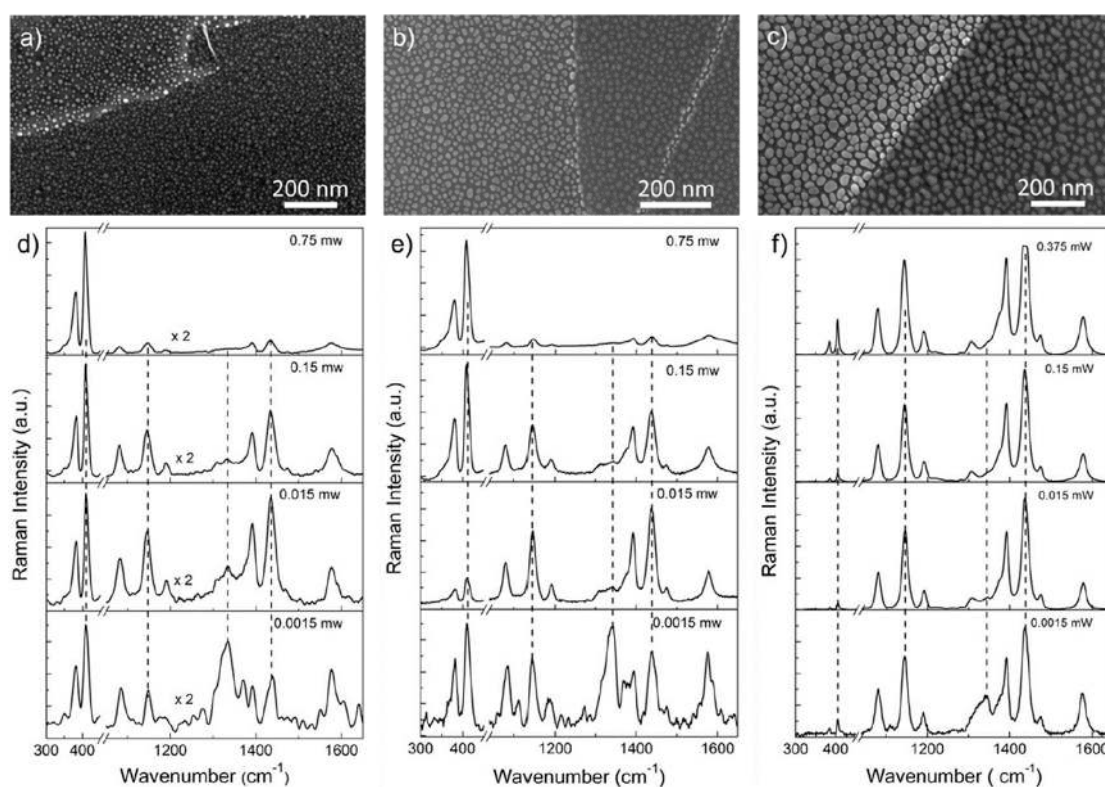

Figure 9. (**a**–**c**) The SEM images of MoS$_2$-Ag NPs with different sizes of Ag NPs, and (**d**–**f**) laser power dependent SERS spectra of the MoS$_2$-Ag NPs hybrids that corresponds to 9(**a**–**c**) [111].
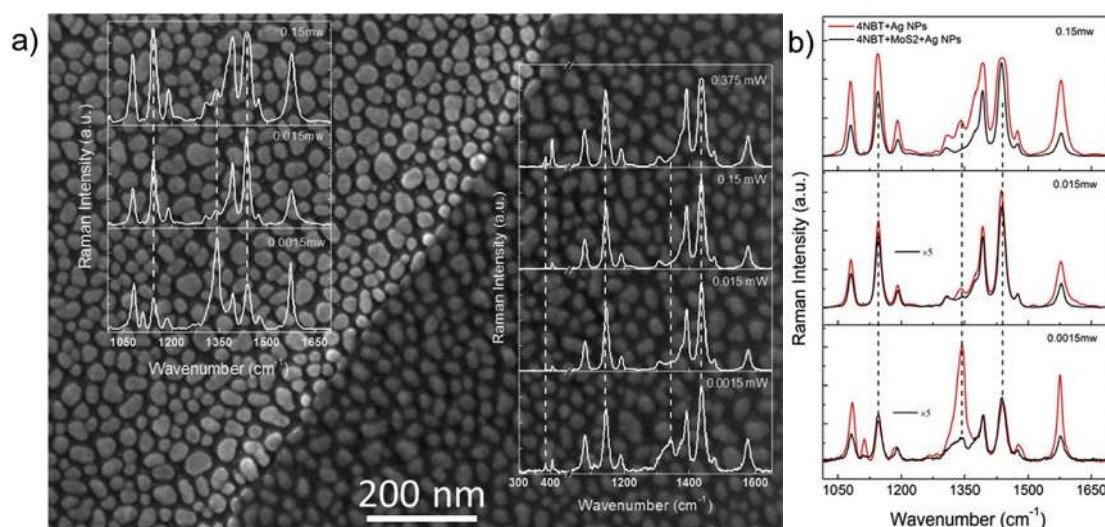

Figure 10. (**a**) The SEM of the Ag substrate, where the right regime is covered by MoS$_2$, and the corresponding surface catalytic reactions in both regimes [111], (**b**) is the SERS spectra.

Also, the physical mechanism of the exciton–plasmon interaction for catalysis has been interpreted theoretically, which revealed ultrafast charge transfer between plasmons and excitons in the hybrid system [112].

4. Conclusions

We reviewed the principle of plasmonic nanostructure–semiconductor exciton interaction and the applications of plasmonic nanostructure–semiconductor exciton interaction for chemical reactions. The exciton–plasmon interaction has greater potential for surface catalytic reactions than plasmon alone. This review can promote a better understanding of the physical mechanism of exciton–plasmon coupling for surface catalysis.

Author Contributions: Investigation, J.W., X.M.; Resources, J.W.; Data Curation, N.F., Y.S.; Writing-Original Draft Preparation, J.W., N.F.; Writing-Review & Editing, J.W., X.M.; Supervision, J.W. and X.M.; Project Administration, J.W., X.M.; Funding Acquisition, J.W.

Conflicts of Interest: The authors declare no conflict of interest.

References

1. Ritchie, R.H. Plasma Losses by Fast Electrons in Thin Films. *Phys. Rev.* **1957**, *106*, 874–881. [CrossRef]
2. Brockman, J.M.; Nelson, B.P.; Corn, R.M. Surface Plasmon Resonance Imaging Measurements of Ultrathin Organic Films. *Annu. Rev. Phys. Chem.* **2000**, *51*, 41–63. [CrossRef] [PubMed]
3. Lin, W.; Cao, Y.; Wang, P.; Sun, M. Unified Treatment for Plasmon–Exciton Co-driven Reduction and Oxidation Reactions. *Langmuir* **2017**, *33*, 12102–12107. [CrossRef] [PubMed]
4. Zhang, Z.L.; Sheng, S.X.; Wang, R.M.; Sun, M.T. Tip-Enhanced Raman Spectroscopy. *Anal. Chem.* **2016**, *88*, 9328–9346. [CrossRef] [PubMed]
5. Viti, L.; Hu, J.; Coquillat, D.; Politano, A.; Knap, W.; Vitiello, M.S. Efficient Terahertz detection in black-phosphorus nano-transistors with selective and controllable plasma-wave, bolometric and thermoelectric response. *Sci. Rep.* **2016**, *6*, 20474. [CrossRef] [PubMed]
6. Ueno, K.; Juodkazis, S.; Shibuya, T.; Yokota, Y.; Mizeikis, V.; Sasaki, K.; Misawa, H. Nanoparticle Plasmon-Assisted Two-Photon Polymerization Induced by Incoherent Excitation Source. *J. Am. Chem. Soc.* **2008**, *130*, 6928–6929. [CrossRef] [PubMed]
7. Hubert, C.; Rumyantseva, A.; Lerondel, G.; Grand, J.; Kostcheev, S.; Billot, L.; Vial, A.; Bachelot, R.; Royer, P.; Chang, S.H.; et al. Near-Field Photochemical Imaging of Noble Metal Nanostructures. *Nano Lett.* **2005**, *5*, 615–619. [CrossRef] [PubMed]
8. Lin, W.; Cao, E.; Zhang, L.; Xu, X.; Song, Y.; Liang, W.; Sun, M. Electrically enhanced hot hole driven oxidation catalysis at the interface of a plasmon-exciton hybrid. *Nanoscale* **2018**, *10*, 5482–5488. [CrossRef] [PubMed]
9. Deeb, C.; Ecoffet, C.; Bachelot, R.; Plain, J.; Bouhelier, A.; Soppera, O. Plasmon-based free-radical photopolymerization: Effect of diffusion on nanolithography processes. *J. Am. Chem. Soc.* **2011**, *133*, 10535–10542. [CrossRef] [PubMed]
10. Sun, M.; Zhang, Z.; Zheng, H.; Xu, H. In-situ plasmon-driven chemical reactions revealed by high vacuum tip-enhanced Raman spectroscopy. *Sci. Rep.* **2012**, *2*, 647. [CrossRef] [PubMed]
11. Chen, C.J.; Osgood, R.M. Direct Observation of the Local-Field-Enhanced Surface Photochemical Reactions. *Phys. Rev. Lett.* **1983**, *50*, 1705–1708. [CrossRef]
12. Fang, Y.; Li, Y.; Xu, H.; Sun, M. Ascertaining p,p'-dimercaptoazobenzene produced from p-aminothiophenol by selective catalytic coupling reaction on silver nanoparticles. *Langmuir* **2010**, *26*, 7737–7746. [CrossRef] [PubMed]
13. Canpean, V.; Iosin, M.; Astilean, S. Disentangling SERS signals from two molecular species: A new evidence for the production of p,p'-dimercaptoazobenzene by catalytic coupling reaction of p-aminothiophenol on metallic nanostructures. *Chem. Phys. Lett.* **2010**, *500*, 277–282. [CrossRef]

14. Sun, M.; Fang, Y.; Zhang, Z.; Xu, H. Activated vibrational modes and Fermi resonance in tip-enhanced Raman spectroscopy. *Phys. Rev. E Stat. Nonlinear Soft Matter Phys.* **2013**, *87*, 020401. [CrossRef] [PubMed]

15. Furube, A.; Du, L.; Hara, K.; Katoh, R.; Tachiya, M. Ultrafast Plasmon-Induced Electron Transfer from Gold Nanodots into TiO_2 Nanoparticles. *J. Am. Chem. Soc.* **2007**, *129*, 14852–14853. [CrossRef] [PubMed]

16. Gabudean, A.M.; Biro, D.; Astilean, S. Localized surface plasmon resonance (LSPR) and surface-enhanced Raman scattering (SERS) studies of 4-aminothiophenol adsorption on gold nanorods. *J. Mol. Struct.* **2011**, *993*, 420–424. [CrossRef]

17. Christopher, P.; Xin, H.; Linic, S. Visible-light-enhanced catalytic oxidation reactions on plasmonic silver nanostructures. *Nat. Chem.* **2011**, *3*, 467. [CrossRef] [PubMed]

18. Cao, E.; Guo, X.; Zhang, L.; Shi, Y.; Lin, W.; Liu, X.; Fang, Y.; Zhou, L.; Sun, Y.; Song, Y. Electrooptical Synergy on Plasmon–Exciton-Codriven Surface Reduction Reactions. *Adv. Mater. Interfaces* **2017**, *4*, 1700869. [CrossRef]

19. Tian, Y.; Tatsuma, T. Mechanisms and Applications of Plasmon-Induced Charge Separation at TiO_2 Films Loaded with Gold Nanoparticles. *J. Am. Chem. Soc.* **2005**, *127*, 7632–7637. [CrossRef] [PubMed]

20. Sun, M.; Zhang, Z.; Wang, P.; Li, Q.; Ma, F.; Xu, H. Remotely excited Raman optical activity using chiral plasmon propagation in Ag nanowires. *Light Sci. Appl.* **2013**, *2*, e112. [CrossRef]

21. Sun, M.; Xu, H. A novel application of plasmonics: Plasmon-driven surface-catalyzed reactions. *Small* **2012**, *8*, 2777–2786. [CrossRef] [PubMed]

22. Politano, A.; Argurio, P.; Di, P.G.; Sanna, V.; Cupolillo, A.; Chakraborty, S.; Arafat, H.A.; Curcio, E. Photothermal Membrane Distillation for Seawater Desalination. *Adv. Mater.* **2017**, *29*, 1603504. [CrossRef] [PubMed]

23. Wang, Q.H.; Kalantar-Zadeh, K.; Kis, A.; Coleman, J.N.; Strano, M.S. Electronics and optoelectronics of two-dimensional transition metal dichalcogenides. *Nat. Nanotechnol.* **2012**, *7*, 699–712. [CrossRef] [PubMed]

24. Kuc, A.; Zibouche, N.; Heine, T. Influence of quantum confinement on the electronic structure of the transition metal sulfide TS_2. *Phys. Rev. B* **2011**, *83*, 2237–2249. [CrossRef]

25. Wilson, J.A.; Yoffe, A.D. The transition metal dichalcogenides discussion and interpretation of the observed optical, electrical and structural properties. *Adv. Phys.* **1969**, *18*, 193–335. [CrossRef]

26. Lana-Villarreal, T.; Gómez, R. Tuning the photoelectrochemistry of nanoporous anatase electrodes by modification with gold nanoparticles: Development of cathodic photocurrents. *Chem. Phys. Lett.* **2005**, *414*, 489–494. [CrossRef]

27. Kowalska, E.; Mahaney, O.O.; Abe, R.; Ohtani, B. Visible-light-induced photocatalysis through surface plasmon excitation of gold on titania surfaces. *Phys. Chem. Chem. Phys.* **2010**, *12*, 2344–2355. [CrossRef] [PubMed]

28. Toyoda, T.; Tsugawa, S.; Shen, Q. Photoacoustic spectra of Au quantum dots adsorbed on nanostructured TiO_2 electrodes together with the photoelectrochemical current characteristics. *J. Appl. Phys.* **2009**, *105*, 034314. [CrossRef]

29. Kowalska, E.; Abe, R.; Ohtani, B. Visible light-induced photocatalytic reaction of gold-modified titanium(IV) oxide particles: Action spectrum analysis. *Chem. Commun.* **2009**, 241–243. [CrossRef] [PubMed]

30. Gong, D.; Weng, C.J.H.; Tang, Y.; Tay, Q.; Lai, Y.; Highfield, J.G.; Chen, Z. Silver decorated titanate/titania nanostructures for efficient solar driven photocatalysis. *J. Solid State Chem.* **2012**, *189*, 117–122. [CrossRef]

31. Tanaka, A.; Ogino, A.; Iwaki, M.; Hashimoto, K.; Ohnuma, A.; Amano, F.; Ohtani, B.; Kominami, H. Gold-titanium(IV) oxide plasmonic photocatalysts prepared by a colloid-photodeposition method: Correlation between physical properties and photocatalytic activities. *Langmuir* **2012**, *28*, 13105–13111. [CrossRef] [PubMed]

32. Ingram, D.B.; Christopher, P.; Bauer, J.L.; Linic, S. Predictive Model for the Design of Plasmonic Metal/Semiconductor Composite Photocatalysts. *ACS Catal.* **2011**, *1*, 1441–1447. [CrossRef]

33. Fujishima, A.; Honda, K. Electrochemical Photolysis of Water at a Semiconductor Electrode. *Nature* **1972**, *238*, 37–38. [CrossRef] [PubMed]

34. Fujishima, A.; Rao, T.N.; Tryk, D.A. Titanium dioxide photocatalysis. *J. Photochem. Photobiol. C Photochem. Rev.* **2000**, *1*, 1–21. [CrossRef]

35. Nazeeruddin, M.K.; Kay, A.; Rodicio, I.; Humphrybaker, R.; Mueller, E.; Liska, P.; Vlachopoulos, N.; Graetzel, M. Conversion of Light to Electricity by cis-XzBis(2,2'-bipyridyl-4,4'-dicarboxylate)ruthenium(II) Charge-Transfer Sensitizers (X = C1$^-$, Br$^-$, I$^-$, CN$^-$, and SCN$^-$) on Nanocrystalline Ti0$_2$ Electrodes. *J. Am. Chem. Soc.* **1993**, *115*, 6382–6390. [CrossRef]

36. Chen, Z.H.; Tang, Y.B.; Liu, C.P.; Leung, Y.H.; Yuan, G.D.; Chen, L.M.; Wang, Y.Q.; Bello, I.; Zapien, J.A.; Zhang, W.J. Vertically Aligned ZnO Nanorod Arrays Sentisized with Gold Nanoparticles for Schottky Barrier Photovoltaic Cells. *J. Phys. Chem. C* **2009**, *113*, 13433–13437. [CrossRef]

37. Liu, W.; Lin, W.; Zhao, H.; Wang, P.; Sun, M. The nature of plasmon-exciton codriven surface catalytic reaction. *J. Raman Spectrosc.* **2018**, *49*, 383–387. [CrossRef]

38. Kamat, P.V. Photochemistry on Nonreactive and Reactive (Semiconductor) Surfaces. *Chem. Rev.* **1993**, *93*, 267–300. [CrossRef]

39. Hoffmann, M.R.; Martin, S.T.; Choi, W.; Bahnemannt, D.W. Environmental Applications of Semiconductor Photocatalysis. *Chem. Rev.* **1995**, *95*, 69–96. [CrossRef]

40. Linsebigler, A.L.; Lu, G.; Yates, J.T. Photocatalysis on TiOn Surfaces: Principles, Mechanisms, and Selected Results. *Chem. Rev.* **1995**, *95*, 735–758. [CrossRef]

41. Vinodgopal, K.; Bedja, I.; Hotchandani, S.; Kamat, P.V. A Photocatalytic Approach for the Reductive Decolorization of Textile Azo Dyes in Colloidal Semiconductor Suspensions. *Langmuir* **1994**, *10*, 1767–1771. [CrossRef]

42. Bahnemann, D.; Henglein, A.; Lilie, J.; Spanhel, L. Flash Photolysis Observation of the Absorption Spectra of Trapped Positive Holes and Electrons in Colloidal TiO$_2$. *J. Phys. Chem.* **1984**, *88*, 709–711. [CrossRef]

43. Gaoa, R.; Safranyc, A.; Rabania, J. Fundamental reactions in TiO$_2$ nanocrystallite aqueous solutions studied by pulse radiolysis. *Radiat. Phys. Chem.* **2002**, *65*, 599–609. [CrossRef]

44. Colombo, D.P., Jr.; Roussel, K.A.; Saeh, J.; Skinner, D.E.; Cavaleri, J.J.; Bowman, R.M. Femtosecond study of the intensity dependence of electron-hole dynamics in TiO$_2$ nanoclusters. *Chem. Phys. Lett.* **1995**, *232*, 207–214. [CrossRef]

45. Ramakrishna, G.; Ghosh, H.N. Optical and Photochemical Properties of Sodium Dodecylbenzenesulfonate (DBS)-Capped TiO$_2$ Nanoparticles Dispersed in Nonaqueous Solvents. *Langmuir* **2003**, *19*, 505–508. [CrossRef]

46. Christopher, P.; Ingram, D.B.; Linic, S. Enhancing Photochemical Activity of Semiconductor Nanoparticles with Optically Active Ag Nanostructures: Photochemistry Mediated by Ag Surface Plasmons. *J. Phys. Chem. C* **2010**, *114*, 9173–9177. [CrossRef]

47. Lin, W.; Xu, X.; Quan, J.; Sun, M. Propagating surface plasmon polaritons for remote excitation surface-enhanced Raman scattering spectroscopy. *Appl. Spectrosc. Rev.* **2018**, *53*, 771–782. [CrossRef]

48. Wang, J.; Tafen, D.N.; Lewis, J.P.; Hong, Z.; Manivannan, A.; Zhi, M.; Li, M.; Wu, N. Origin of Photocatalytic Activity of Nitrogen-Doped TiO$_2$ Nanobelts. *J. Am. Chem. Soc.* **2009**, *131*, 12290–12297. [CrossRef] [PubMed]

49. Ohno, T.; Sarukawa, K.; Tokieda, K.; Matsumura, M. Morphology of a TiO$_2$ Photocatalyst (Degussa, P-25) Consisting of Anatase and Rutile Crystalline Phases. *J. Catal.* **2001**, *203*, 82–86. [CrossRef]

50. Fujishima, A.; Zhang, X.; Tryk, D. TiO$_2$ photocatalysis and related surface phenomena. *Surf. Sci. Rep.* **2008**, *63*, 515–582. [CrossRef]

51. Zhu, K.; Neale, N.R.; Miedaner, A.; Frank, A.J. Enhanced Charge-Collection Efficiencies and Light Scattering in Dye-Sensitized Solar Cells Using Oriented TiO$_2$ Nanotubes Arrays. *Nano Lett.* **2007**, *7*, 69–74. [CrossRef] [PubMed]

52. Ding, Q.; Shi, Y.; Chen, M.; Li, H.; Yang, X.; Qu, Y.; Liang, W.; Sun, M. Ultrafast Dynamics of Plasmon-Exciton Interaction of Ag Nanowire- Graphene Hybrids for Surface Catalytic Reactions. *Sci. Rep.* **2016**, *6*, 32724. [CrossRef] [PubMed]

53. Fofang, N.T.; Grady, N.K.; Fan, Z.; Govorov, A.O.; Halas, N.J. Plexciton dynamics: Exciton-plasmon coupling in a J-aggregate-Au nanoshell complex provides a mechanism for nonlinearity. *Nano Lett.* **2011**, *11*, 1556–1560. [CrossRef] [PubMed]

54. Wiederrecht, G.P.; Wurtz, G.A.; Hranisavljevic, J. Coherent Coupling of Molecular Excitons to Electronic Polarizations of Noble Metal Nanoparticles. *Nano Lett.* **2004**, *4*, 2121–2125. [CrossRef]

55. Wurtz, G.A.; Evans, P.R.; Hendren, W.; Atkinson, R.; Dickson, W.; Pollard, R.J.; Zayats, A.V.; Harrison, W.; Bower, C. Molecular Plasmonics with Tunable Exciton−Plasmon Coupling Strength in J-Aggregate Hybridized Au Nanorod Assemblies. *Nano Lett.* **2007**, *7*, 1297–1303. [CrossRef] [PubMed]

56. Govorov, A.O.; Bryant, G.W.; Zhang, W.; Skeini, T.; Lee, J.; Kotov, N.A.; Slocik, J.M.; Naik, R.R. Exciton−Plasmon Interaction and Hybrid Excitons in Semiconductor−Metal Nanoparticle Assemblies. *Nano Lett.* **2006**, *6*, 984–994. [CrossRef]

57. Bellessa, J.; Symonds, C.; Vynck, K.; Beaur, L.; Brioude, A.; Lemaitre, A. Giant Rabi splitting in metal/semiconductor nanohybrids. *Superlattices Microstruct.* **2011**, *49*, 209–216. [CrossRef]

58. Bishnoi, S.W.; Rozell, C.J.; Levin, C.S.; Gheith, M.K.; Johnson, B.R.; Johnson, D.H.; Halas, N.J. All-Optical Nanoscale pH Meter. *Nano Lett.* **2006**, *6*, 1687–1692. [CrossRef] [PubMed]

59. Govorov, A.O.; Carmeli, I. Hybrid Structures Composed of Photosynthetic System and Metal Nanoparticles: Plasmon Enhancement Effect. *Nano Lett.* **2007**, *7*, 620–625. [CrossRef] [PubMed]

60. Wang, J.; Xu, X.; Mu, X.; Ma, F.; Sun, M. Magnetics and spintronics on two-dimensional composite materials of graphene/hexagonal boron nitride. *Mater. Today Phys.* **2017**, *3*, 93–117. [CrossRef]

61. Artuso, R.D.; Bryant, G.W. Optical Response of Strongly Coupled Quantum Dot-Metal Nanoparticle Systems: Double Peaked Fano Structure and Bistability. *Nano Lett.* **2008**, *8*, 2106–2111. [CrossRef] [PubMed]

62. Purcell, E.M. *Confined Electrons and Photons: New Physics and Applications*; Burstein, E., Weisbuch, C., Eds.; Springer: New York, NY, USA, 1995; p. 839.

63. Bharadwaj, P.; Deutsch, B.; Novotny, L. Optical Antennas. *Adv. Opt. Photonics* **2009**, *1*, 438–483. [CrossRef]

64. Henkel, C.; Sandoghdar, V. Single-molecule spectroscopy near structured dielectrics. *Opt. Commun.* **1998**, *158*, 250–262. [CrossRef]

65. Kuhn, H. Classical Aspects of Energy Transfer in Molecular Systems. *J. Chem. Phys.* **1970**, *53*, 101–108. [CrossRef]

66. Yeung, M.S.; Gustafson, T.K. Spontaneous emission near an absorbing dielectric surface. *Phys. Rev. A* **1996**, *54*, 5227–5242. [CrossRef] [PubMed]

67. Giannini, V.; Fernandez-Dominguez, A.I.; Heck, S.C.; Maier, S.A. Plasmonic nanoantennas: Fundamentals and their use in controlling the radiative properties of nanoemitters. *Chem. Rev.* **2011**, *111*, 3888–3912. [CrossRef] [PubMed]

68. Savasta, S.; Saija, R.; Ridolfo, A.; Di, S.O.; Denti, P.; Borghese, F. Nanopolaritons: Vacuum Rabi Splitting with a Single Quantum Dot in the Center ofa Dimer Nanoantenna. *ACS Nano* **2010**, *4*, 6369–6376. [CrossRef] [PubMed]

69. Berman, P.R. *Cavity Quantum Electrodynamics*; Academic Press, Inc.: Boston, MA, USA, 1994.

70. Vahala, K.J. Optical microcavities. *Nature* **2003**, *424*, 839–846. [CrossRef] [PubMed]

71. Giannini, V.; Sánchez-Gil, J.A.; Muskens, O.L.; Rivas, J.G. Electrodynamic calculations of spontaneous emission coupled to metal nanostructures of arbitrary shape: Nanoantenna-enhanced fluorescence. *J. Opt. Soc. Am. B* **2009**, *26*, 1569–1577. [CrossRef]

72. Maier, S.A. *Plasmonics: Fundamentals and Applications*; Springer: Berlin/Heidelberg, Germany, 2007.

73. Manjavacas, A.; Garcia de Abajo, F.J.; Nordlander, P. Quantum plexcitonics: Strongly interacting plasmons and excitons. *Nano Lett.* **2011**, *11*, 2318–2323. [CrossRef] [PubMed]

74. Schlather, A.E.; Large, N.; Urban, A.S.; Nordlander, P.; Halas, N.J. Near-field mediated plexcitonic coupling and giant Rabi splitting in individual metallic dimers. *Nano Lett.* **2013**, *13*, 3281–3286. [CrossRef] [PubMed]

75. Tischler, J.R.; Bradley, M.S.; Zhang, Q.; Atay, T.; Nurmikko, A.; Bulović, V. Solid state cavity QED: Strong coupling in organic thin films. *Org. Electron.* **2007**, *8*, 94–113. [CrossRef]

76. McFarland, E.W.; Tang, J. Aphotovoltaicdevicestructure based on internal electron emission. *Nature* **2003**, *421*, 616–618. [CrossRef] [PubMed]

77. Fang, Y.; Zhang, Z.; Sun, M. High vacuum tip-enhanced Raman spectroscope based on a scanning tunneling microscope. *Rev. Sci. Instrum.* **2016**, *87*, 033104. [CrossRef] [PubMed]

78. Zhao, G.; Kozuka, H.; Yoko, T. Sol-gel preparation and photoelectrochemical properties ofTiO_2 containing Au and Ag metal particles. *Thin Solid Films* **1996**, *277*, 147–154. [CrossRef]

79. Li, H.; Bian, Z.; Zhu, J.; Huo, Y.; Li, H.; Lu, Y. Mesoporous Au/TiO_2 nanocomposites with enhanced photocatalytic activity. *J. Am. Chem. Soc.* **2007**, *129*, 4538–4539. [CrossRef] [PubMed]

80. Sönnichsen, C.; Raschke, G.; Plessen, G.V.; Feldmann, J.; Wilson, O.; Mulvaney, P.; Franzl, T.; Wilk, T. Drastic reduction of plasmon damping in gold nanorods. *Phys. Rev. Lett.* **2002**, *88*, 077402. [CrossRef] [PubMed]

81. Lehmann, J.; Merschdorf, M.; Pfeiffer, W.; Thon, A.; Voll, S.; Gerber, G. Surface Plasmon Dynamics in Silver Nanoparticles Studied by Femtosecond Time-Resolved Photoemission. *Phys. Rev. Lett.* **2000**, *85*, 2921–2924. [CrossRef] [PubMed]

82. Hofmann, J.; Steinmann, W. Plasma Resonance in the Photoemission of Silver. *Phys. Stat. Sol.* **1968**, *30*, K53–K56. [CrossRef]

83. Endriz, J.G.; Spicer, W.E. Surface-Plasmon-One-Electron Decay and its Observation in Photoemission. *Phys. Rev. Lett.* **1970**, *24*, 64–68. [CrossRef]

84. Ding, Q.; Chen, M.; Fang, Y.; Zhang, Z.; Sun, M. Plasmon-Driven Diazo Coupling Reactions of p-Nitroaniline via $-NH_2$ or $-NO_2$ in Atmosphere Environment. *J. Phys. Chem. C* **2017**, *121*, 5225–5231. [CrossRef]

85. Wang, J.; Lin, W.; Xu, X.; Ma, F.; Sun, M. Plasmon-Exciton Coupling Interaction for Surface Catalytic Reactions. *Chem. Rec.* **2018**, *18*, 481–490. [CrossRef] [PubMed]

86. Du, L.; Furube, A.; Yamamoto, K.; Hara, K.; Katoh, R.; Tachiya, M. Plasmon-Induced Charge Separation and Recombination Dynamics in Gold-TiO_2 Nanoparticle Systems: Dependence on TiO_2 Particle Size. *J. Phys. Chem. C* **2009**, *113*, 6454–6462. [CrossRef]

87. Duonghong, D.; Ramsden, J.; Gratzel, M. Dynamics of Interfacial Electron-Transfer Processes in Colloidal Semiconductor Systems. *J. Am. Chem. Soc.* **1982**, *104*, 2977–2985. [CrossRef]

88. Arbour, C.; Sharma, D.K.; Langford, C.H. Picosecond Flash Spectroscopy of TiO_2, Colloids with Adsorbed Dyes. *J. Phys. Chem.* **1990**, *94*, 331–335. [CrossRef]

89. Rothenberger, G.; Moser, J.; Gratzel, M.; Serpone, N.; Sharma, D.K. Charge Carrier Trapping and Recombination Dynamics in Small Semiconductor Particles. *J. Am. Chem. Soc.* **1985**, *107*, 8054–8059. [CrossRef]

90. Kolle, U.; Moser, J.; Gratzel, M. Dynamics of Interfacial Charge-Transfer Reactions in Semiconductor Dispersions. Reduction of Cobaltoceniumdicarboxylate in Colloidal TiO_2. *Inorg. Chem.* **1985**, *24*, 2253–2258. [CrossRef]

91. Arbour, C.; Sharma, D.K.; Langford, C.H. Kinetics of electron build-up in TiO_2 colloids probed by hole scavenging after picosecond excitation. *Chem. Commun.* **1987**, 917–918. [CrossRef]

92. Bahnemann, D.; Henglein, A.; Spanhel, L. Detection of the intermediates of colloidal TiO_2-catalysed photoreactions. *Faraday Discuss. Chem. Soc.* **1984**, *78*, 151–163. [CrossRef]

93. Bahnemann, D.W.; Hilgendorff, M.; Memming, R. Charge Carrier Dynamics at TiO_2 Particles: Reactivity of Free and Trapped Holes. *J. Phys. Chem. B* **1997**, *101*, 4265–4275. [CrossRef]

94. Li, R.; Zhang, Y.; Xu, X.; Zhou, Y.; Chen, M.; Sun, M. Optical characterizations of two-dimensional materials using nonlinear optical microscopies of CARS, TPEF, and SHG. *Nanophotonics* **2018**, *7*, 873–881. [CrossRef]

95. Dimitrijevic, N.M.; Saponjic, Z.V.; Bartels, D.M.; Thurnauer, M.C.; And, D.M.T.; Rajh, T. Revealing the Nature of Trapping Sites in Nanocrystalline Titanium Dioxide by Selective Surface Modification. *J. Phys. Chem. B* **2003**, *107*, 7368–7375. [CrossRef]

96. Rabani, J.; Yamashita, K.; Ushida, K.; Stark, J.; Kira, A. Fundamental Reactions in Illuminated Titanium Dioxide Nanocrystallite Layers Studied by Pulsed Laser. *J. Phys. Chem. B* **1998**, *102*, 1689–1695. [CrossRef]

97. Asahi, T.; Furube, A.; Masuhara, H. Direct measurement of picosecond interfacial electron transfer from photoexcited TiO_2 powder to an adsorbed molecule in the opaque suspension. *Chem. Phys. Lett.* **1997**, *275*, 234–238. [CrossRef]

98. Brongersma, M.L.; Halas, N.J.; Nordlander, P. Plasmon-induced hot carrier science and technology. *Nat. Nanotechnol.* **2015**, *10*, 25–34. [CrossRef] [PubMed]

99. Harutyunyan, H.; Martinson, A.B.; Rosenmann, D.; Khorashad, L.K.; Besteiro, L.V.; Govorov, A.O.; Wiederrecht, G.P. Anomalous ultrafast dynamics of hot plasmonic electrons in nanostructures with hot spots. *Nat. Nanotechnol.* **2015**, *10*, 770–774. [CrossRef] [PubMed]

100. Link, S.; El-Sayed, M.A. Spectral Properties and Relaxation Dynamics of Surface Plasmon Electronic Oscillations in Gold and Silver Nanodots and Nanorods. *J. Phys. Chem. B* **1999**, *103*, 8410–8426. [CrossRef]

101. Link, S.; El-Sayed, M.A. Shape and size dependence of radiative, non-radiative and photothermal properties of gold nanocrystals. *Int. Rev. Phys. Chem.* **2000**, *19*, 409–453. [CrossRef]

102. Katoh, R.; Furube, A.; Yoshihara, T.; Hara, K.; Fujihashi, G.; Takano, S.; Murata, S.; Arakawa, H.; Tachiya, M. Efficiencies of Electron Injection from Excited N3 Dye into Nanocrystalline Semiconductor (ZrO_2, TiO_2, ZnO, Nb_2O_5, SnO_2, In_2O_3) Films. *J. Phys. Chem. B* **2004**, *108*, 4818–4822. [CrossRef]

103. Tian, Y.; Wang, X.; Zhang, D.; Shi, X.; Wang, S. Effects of electron donors on the performance of plasmon-induced photovoltaic cell. *J. Photochem. Photobiol. A Chem.* **2008**, *199*, 224–229. [CrossRef]

104. Wang, J.; Ma, F.; Liang, W.; Sun, M. Electrical properties and applications of graphene, hexagonal boron nitride (h-BN), and graphene/h-BN heterostructures. *Mater. Today Phys.* **2017**, *2*, 6–34. [CrossRef]

105. Lin, W.; Shi, Y.; Yang, X.; Li, J.; Cao, E.; Xu, X.; Pullerits, T.; Liang, W.; Sun, M. Physical Mechanism on Exciton-Plasmon Coupling Revealed by Femtosecond Pump-Probe Transient Absorption Spectroscopy. *Mater. Today Phys.* **2017**, *3*, 33–40. [CrossRef]

106. Quan, J.; Cao, E.; Mu, X.; Sun, M. Surface catalytic reaction driven by plasmonic waveguide. *Appl. Mater. Today* **2018**, *11*, 50–56. [CrossRef]

107. Zhang, Z.; Xu, P.; Yang, X.; Liang, W.; Sun, M. Surface plasmon-driven photocatalysis in ambient, aqueous and high-vacuum monitored by SERS and TERS. *J. Photochem. Photobiol. C Photochem. Rev.* **2016**, *27*, 100–112. [CrossRef]

108. Mubeen, S.; Lee, J.; Singh, N.; Krämer, S.; Stucky, G.D.; Moskovits, M. An autonomous photosynthetic device in which all charge carriers derive from surface plasmons. *Nat. Nanotechnol.* **2013**, *8*, 247–251. [CrossRef] [PubMed]

109. Ding, Q.; Li, R.; Chen, M.; Sun, M. Ag nanoparticles-TiO$_2$ film hybrid for plasmon-exciton co-driven surface catalytic reactions. *Appl. Mater. Today* **2017**, *9*, 251–258. [CrossRef]

110. Lin, W.; Ren, X.; Cui, L.; Sun, M. Electro-optical tuning of plasmon-driven double reduction interface catalysis. *Appl. Mater. Today* **2018**, *11*, 189–192. [CrossRef]

111. Yang, X.; Yu, H.; Guo, X.; Ding, Q.; Pullerits, T.; Wang, R.; Zhang, G.; Liang, W.; Sun, M. Plasmon-exciton coupling of monolayer MoS$_2$ -Ag nanoparticles hybrids for surface catalytic reaction. *Mater. Today Energy* **2017**, *5*, 72–78. [CrossRef]

112. Xu, X.; Shi, Y.; Liu, X.; Sun, M. Femtosecond dynamics of monolayer MoS$_2$ -Ag nanoparticles hybrid probed at 532 nm. *Chem. Phys. Lett.* **2018**, *692*, 208–213. [CrossRef]